Carbon-reduction as an easy route for the synthesis of VO2 (M1) and further Al, Ti doping

Shian Guan, Manuel Gaudon, Mélanie Souquet-Basiège, Oudomsack Viraphong, Nicolas Penin, Aline Rougier

ARTICLE

DOI: 10.1039/C8DT04914A

Carbon-reduction as easy route for the synthesis of VO_2 (M1) and further Al, Ti doping

Shian Guan, Manuel Gaudon, Mélanie Souquet-Basiège, Oudomsack Viraphong, Nicolas Penin and Aline Rougier*

A low-cost and facile method to synthesize highly crystallized VO_2 (M1) particles is proposed, using carbon black as reducing agent mixed with V_2O_5 nanopowders comparing two types of vacuum systems for the thermal activation. In sealed vacuum system, CO gas is generated in the first reductive step, and continue to reduce the new born VO_2, until all the V (4+) are reduced to V (3+), resulting in V_2O_3 formation at 1000°C. On the contrary, in dynamic vacuum system, CO gas is ejected through pumping as soon as it is generated, leading to the formation of pure VO_2 (M1) at high temperatures (*i.e.* in the range 700°C ≤ T ≤ 1000°C). The evolution of the carbon content, determined by CHNS, of each sample *versus* the synthesis conditions, namely temperature and type of vacuum system, confirms that the transformation of V (5+) to V (4+) or V (3+) can be controlled. The characterization of the morphologies and crystal structures of two synthesized VO_2 (M1) at 700°C and 1000°C shows the possibility to tune the crystallite size from 1.8 to more than 5 µm, with a uniform size distribution and highly crystallized powders. High purity VO_2 (M1) leads to strong physical properties illustrated by a high latent energy (~55 J/g) during the phase transition obtained from DSC as well as high resistivity changes. In addition, with this method, dopants such as Ti^{4+} or Al^{3+} can be successfully introduced into VO_2 (M1) thanks to the preparation of Al or Ti-doped nano-V_2O_5 by co-precipitation in polyol medium before carbon-reduction.

1. Introduction

As a well-known thermochromic material, vanadium dioxide (VO_2) has attracted extensive attention since 1959. [1-2] It exhibits a first-order metal-insulator transition (MIT) from monoclinic phase to rutile phase at critical transition temperature, T_c of about 68°C.

Although investigations on VO_2 smart windows have been carried on a world-wide scale, [3-5] commercial utilization has not yet been achieved. One of the limiting factors is the basic requirement for the synthesis method: large-scale synthesis, precise phase control, low-cost method to introduce homogeneously doping ions in favor of a phase transition temperature control. Many approaches have already been explored to prepare VO_2 particles or films. Chemical and physical techniques are two main categories, gathering processes such as hydrothermal, [6-9] magnetron sputtering, [10-12] CVD, [13, 14] sol-gel, [15] dip-coating, [16-18] *etc*. For industrial fabrication, parameters such as cost, scale, and equipment are usually considered first. Dip-coating is an inexpensive manufacturing process that facilitates large VO_2 film formation among the techniques, which usually require high-quality VO_2 particles that can be dispersed in an aqueous solvent and be casted into films with good visible transmittance and regulation ability of infrared light. However, the synthesis of VO_2 particles with uniform size and high crystallinity is still a challenge, due to the existence of more than one vanadium oxidation states, such as V^{3+}, V^{4+} and V^{5+}, that easily causes the formation of nonstoichiometric vanadium oxides as well as the stability of V_2O_5. The latter is a well-known candidate for battery application [19]. To optimize the thermochromic properties, *i.e.* to adjust the phase transition between opaque and transparent states around the room temperature, an additional challenge is the production of metal doped-VO_2 particles with a uniform distribution and well-controlled doping concentration.

To synthesize VO_2, intermediate phase transformation is the main strategy however some researches pay attention to another strategy, namely the redox reaction, which is usually applied in the hydrothermal method. Reducing agents (oxalic acid, diamide hydrochloride, or ethylene glycol, *etc.*) are often used, including for the reduction of pentavalent vanadium compounds (V_2O_5 or NH_4VO_3) as raw materials, always leading to a non-spherical (*i.e.* snowflake) shapes. [4, 7, 8] In addition, the use of reducing gas (*e.g.* H_2, CO, C_2H_4, and CO_2) is also reported. [20-22] Nevertheless, disadvantages linked to the use of combustible gas, large energy consumption, toxicity, and cost production favor the utilization of a solid reducing agent. As far as we know, only few researches have focused on mixing directly in furnaces reducing solid agent with high valence vanadium compounds. [24]

Vanadyl ethylene glycolate (VEG) is a popular vanadium precursor, [12, 25] which is mainly used to synthesize VO_2 or V_2O_5. Recently, our team has successfully synthesized high crystallized nano-V_2O_5 *via* a single thermal treatment under air at intermediate temperature and VO_2 (M1) via two-step thermolysis and annealing of VEG, the VEG precursor being prepared by polyol process. Interestingly, it was found that the carbon acts as a reducing agent on the formation of VO_2 (M1). [26] Inspired by these observations, herein soot (carbon) is chosen for a direct reduction of nano V_2O_5. The comparison of dynamic and sealed vacuum systems associated with an accurate control of the carbon contents allows further understanding of the reductive mechanism. Finally, the highly crystallized VO_2 (M1) particles are successfully synthesized through this simple method showing nice physical properties. Besides, their morphologies and phase transition properties are also studied. Improvement of the thermochromic properties are often associated with doping.

[a] *CNRS, Univ. Bordeaux, ICMCB UMR 5026, Pessac, F-33600, France*

† Footnotes relating to the title and/or authors should appear here.

Electronic Supplementary Information (ESI) available: [details of any supplementary information available should be included here]. See DOI: 10.1039/ C8DT04914A

Ensuring the homogenization of aluminum or titanium cation in VO_2 by solid state synthesis is an expensive challenge requiring very high temperatures due to the high melting point of aluminum or titanium oxides (about 2000°C). Thus Ti-doping and Al-doping are school case examples of two doping elements which are very difficult to homogeneously introduce in another oxide matrix using solid state synthesis and that could benefit from the polyol synthesis process. Ti^{4+} and Al^{3+} are introduced in polyol medium to evaluate the doping possibilities of this method. Ti^{4+} ion, isovalent to V^{4+} can be introduced in VO_2 and no electron transfer occurs between Ti^{4+} and V^{4+} ions. For Al^{3+} doping, it is very meaningful to develop a controllable and reliable method of producing Al-doped VO_2 since it leads to the access of the M2 phase, which is an intermediate phase between the M1-R transition. [27, 28] As a Mott insulator, M2 phase can transform to a metallic phase upon carrier injection, showing potential applications in Mott field-effect transistor.

2. Experimental

2.1. Precursors

Ammonium metavanadate (NH_4VO_3; 99.0%), ethylene glycol ($C_2H_6O_2$), Soot (Carbon black, S. A. 75 m^2/g; Bulk density: 80-120g/L), were purchased from PROLABO, Sigma Aldrich and Alfa Aesar Co, respectively. Titanium oxychloride ($TiOCl_2$) and Aluminium isopropoxide Al(O-i-Pr) were purchased from Sigma Aldrich. All the chemicals reagents were used as obtained commercially without further purification.

2.2. Synthesis

The VO_2 synthesis route is schematized in the **Fig. 1a.** Vanadyl ethylene glycolate (VEG: $VC_2H_4O_3$) was obtained through polyol process using NH_4VO_3 as vanadium soluble source. The process has already been described in details in our previous work. [26] After being heated at 300°C for 90 minutes in air, nano V_2O_5 is prepared. Then various molar ratios of soot are mixed with the as-synthesized V_2O_5 (*i.e.* V_2O_5: C molar ratios =1:0, 1:0.5, 1:1, 1:2 and 1:10), which are named as S-0, S-1, S-2, S-3 and S-4, respectively. The mixtures are further annealed at 500°C for 5 h in sealed vacuum system (SVS), as shown in **Fig. 1b** (leading to SVS-1, SVS-2, SVS-3 and SVS-4 samples)**.** SVS is designed by sealing the glass tube after being pumped to vacuum environment (~10^{-4} mbar). S-2 sample is further annealed to high temperatures (700°C and 1000°C) in this system (the impact of temperatures is studied between the as-called SVS-500, SVS-700, and SVS-1000). As a comparison in **Fig. 1c**, the dynamic vacuum system (DVS) is designed for pumping the glass tube during the whole annealing process. For this DVS system, only a V_2O_5: C molar ratio =1: 1 is used (S-2 sample), and thermal treatments at 500°C, 700°C and 1000°C for 15 h are used (leading to DVS-500, DVS-700 and DVS-1000 samples, respectively). It should be mentioned that the two vacuum pressures are controlled the same (~10^{-4} mbar).

Al-doped VO_2 (target composition of 10 at%) and Ti-doped VO_2 samples (target composition of 10 at%) were prepared from the corresponding M-doped VEG precursors, which were synthesized, thanks to the stoichiometric addition of Al(O-*i*-Pr)$_3$ and $TiOCl_2$ besides the NH_4VO_3 in polyol medium, respectively. The two doped precursors were heated at 300°C for 90 min in air. After mixing with carbon black with a molar ratio of 1: 1, the mixtures were both annealed in dynamic vacuum system (DVS) at 700°C for 15 h.

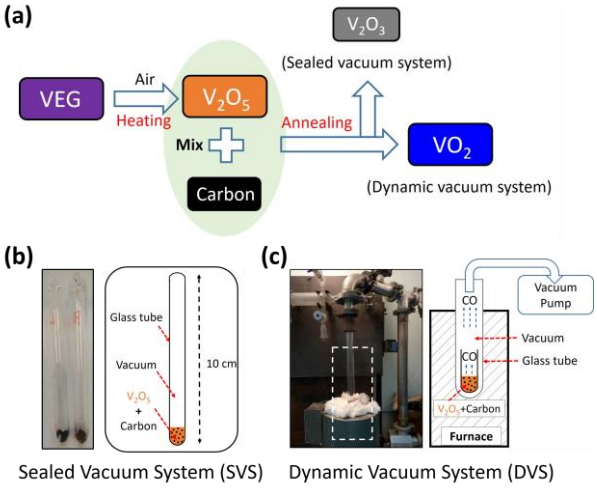

Figure. 1. (a) The different synthesis paths for the preparation of VO_2 or V_2O_3 from the reduction of nano-V_2O_5 by carbon. (b) Sealed vacuum system (SVS): glass tube is sealed after being pumped to vacuum environment; (c) Dynamic vacuum system (DVS): glass tube is pumped during the whole annealing process to maintain the vacuum environment.

2.3. Characterizations

The crystal structures of the as-prepared samples were determined by X-ray diffraction (XRD) analyses (Philips PW1820, PANalytical X' Pert PRO MPD diffractometer) performed using Cu-Kα1 radiation source (λ=1.54056 Å), with divergent slit of 1° and receiving slit size of 0.1 mm in a 2θ range from 8° to 80°. The phase identification was deduced from the comparison of the experimental XRD patterns to standards compiled by the Joint Committee on Powder Diffraction and Standards. Moreover, Rietveld refinements were performed using FullProf software. The morphology of the as-prepared particles was observed by SEM using a TESCAN Vega II SBH microscope and JEOL JSM-6700F, and by High Resolution Transmission Electron Microscopy (HRTEM, JEOL 2200FS, operating at 200 kV). Carbon content of each sample was determined by CHNS elementary analyzer (Thermo Fisher Scientific). Differential scanning calorimetry (DSC) experiment of as-obtained VO_2 powders was performed using Perkin-Elmer DSC. The doping element content was operated in a 720-ES Inductively Coupled Plasma-Optical Emission Spectrometers (ICP-OES, Varian Inc.).

3. Results and Discussions

3.1. SVS Process: V_2O_5/Carbon ratio optimization

According to our previous study, [26] V_2O_3 powder can be obtained by annealing the VEG precursor directly in inert atmospheres or vacuum environment. V_2O_3 is synthesized when the VEG is annealed at 500°C for 5 h in sealed vacuum system, which is due to the reducibility of carbon from the VEG ($VC_2H_4O_3$). In the meantime, VEG can also be used as vanadium precursor for preparing nano V_2O_5, when heated at 300°C for 90 min in air (**Fig. S1**). After the full decomposition, almost no carbon (0.32 wt%; measured by CHNS) remains in the V_2O_5 powder, while the initial carbon content is 12.42 wt% in the VEG compound. Taking advantage of the reduction power of carbon and

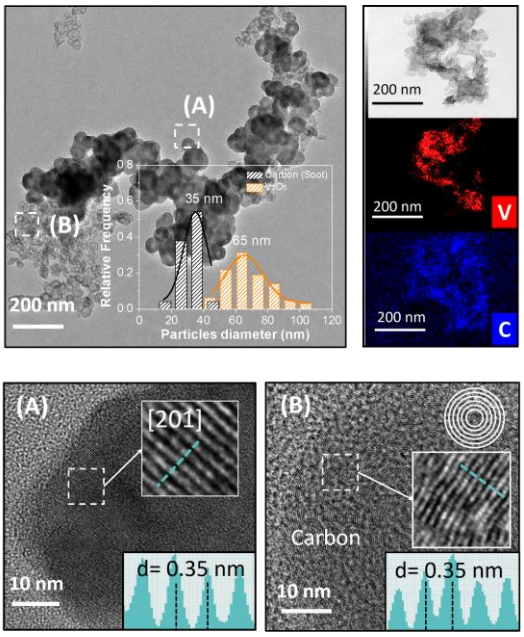

Figure. 2. Top left panel: TEM images of S-2 sample and the extracted particles distribution for V_2O_5 and carbon soot particles; HRTEM images of (A) focus on one V_2O_5 nanoparticle and the corresponding d-spacing of 0.35 nm indexed to [201] plane, (B) focus on a soot particle showing a concentric layered architecture (onion like particle) and the corresponding spacing of 0.35 nm also; Top right panel: TEM elemental mapping (V and C elements) showing the carbon-vanadium homogeneous distribution under the micron scale.

aiming at synthesizing VO_2, herein soot is used as a reducing solid agent starting from nano V_2O_5.

To control the vanadium valences changes from V (5+) to V (4+) or V (3+), the carbon content is carefully and precisely controlled. Various concentrations of soot (*i.e*. V_2O_5: carbon molar ratios = 1:0, 1:0.5, 1:1, 1:2 and 1:10) are grinded with the as-synthesized V_2O_5. The morphology and microstructure of the mixture (S-2 sample) are shown in **Fig. 2**.

Two types of spherical particles co-exist. In A region, the darker ones with larger size are assigned to V_2O_5, with a narrow size distribution around 65 nm. At high magnification, the corresponding d-spacing of around 0.35 nm, can be indexed to [201] plane of orthorhombic V_2O_5 (S.G. Pmmn, JCPDS No. 41-1426). In B region, the agglomerated structure composed of smaller spherical primary particles (~35 nm) with a light color, are typical of the soot morphology. [29, 30] Focusing on one soot particle, an onion-like carbon nanostructures consisting of a continuous network of concentric, size-limited graphene layers is observed, while the characteristic nanostructure is visible with 0.35 nm d-spacing. Young-jin Ko et al also reported that this onion-like carbon could act as an electrocatalyst for $[VO]^{2+}/[VO_2]^{+}$ redox flow reaction. [30] The elemental mapping images show a uniform distribution under the micron scale of V and C components, which could guarantee the full reduction process during the annealing treatment.

The X-ray pattern of the SVS samples obtained after annealing at 500°C for 5 h in sealed vacuum system are gathered in **Fig. 3**. Without carbon, the X-ray pattern of SVS-0 indicates the crystallization of a pure V_2O_5 phase. After carbon addition, V_3O_7 phase appears in the SVS-1 sample, indicating that parts of V (5+) is reduced to V (4+) in this intermediate state between V_2O_5 and VO_2. Further increase in carbon content leads to a relatively pure VO_2 (M1) phase for SVS-2, SVS-3 and SVS-4 samples, the main XRD peaks match with VO_2's JCPDS data card 00-044-0252. Meanwhile, trace of undesired V_6O_{13} impurity is detectable (*i.e.* XRD peak located at 25°). Unexpectedly, the X-ray patterns are not further modified for a large increase in carbon content (*i.e.* comparing to SVS-2, SVS-3 and SVS-4). No additional peaks or intensity increase of vanadium V (3+) compounds are being detected suggesting that V_6O_{13} trace does not result from an excessive carbon-reduction leading VO_2 to further V_6O_{13} transformation but more surely from a parasite reaction occurring at the beginning of the process. Even when a quite large quantity of carbon is added (*i.e.* SVS-4 sample, V_2O_5: C=1: 10), VO_2 phase is prepared using this process. We assume that the relative low annealing temperature of 500°C probably limits the further reduction from V (4+) to V (3+).

Since carbon plays a critical role in the preparation of VO_2 powder and to conclude on the carbo-reduction mechanism, carbon weight fractions of SVS samples were measured before and after annealing (**Fig. 4**). Herein, V_2O_5: C molar ratios are converted in carbon wt%. For example, V_2O_5: C molar ratios =1: 1, which equals the carbon weight percentage is around 6.19 wt%. For SVS-1 sample, still 2.59 wt% of carbon remains in the powder from initial 3.21 wt%. Thus around 0.62 wt% is consumed during the reductive reaction, resulting in the formation of V_3O_7 (**Fig. 3**). For the SVS-2 sample, the difference of carbon weight fraction during the annealing process is around 2.0%, and it remains unchanged for SVS-3 and SVS-4 samples, which indicates that excess of carbon in fact does not take part in the reductive reaction. The fractions of consumed carbon in the CHNS result well agree with the XRD results (**Fig. 3**), revealing

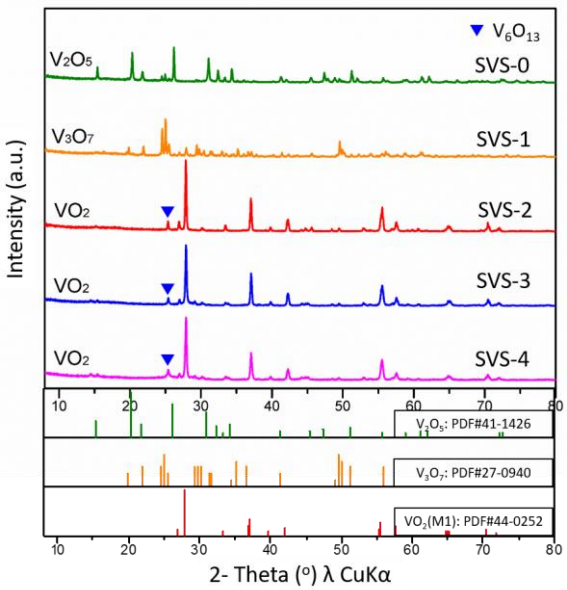

Figure. 3. XRD patterns of SVS samples synthesized by annealing of nano-V_2O_5 mixed with various carbon contents at 500°C for 5 h in sealed vacuum system. Corresponding PDF numbers provided at the bottom.

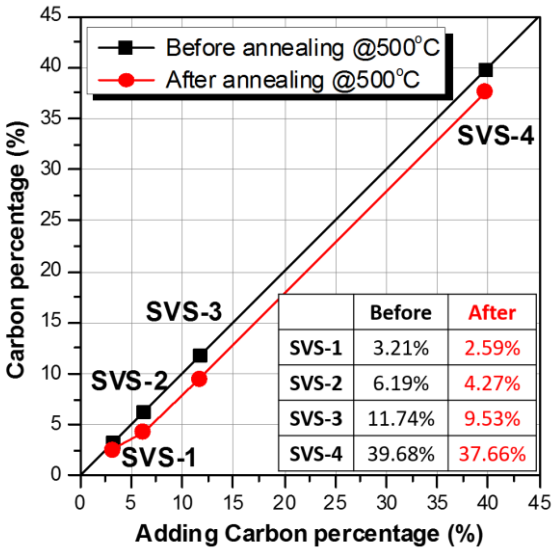

Figure. 4. Carbon wt. percentages of samples before and after annealing at 500°C in sealed vacuum system (SVS) for 5 h.

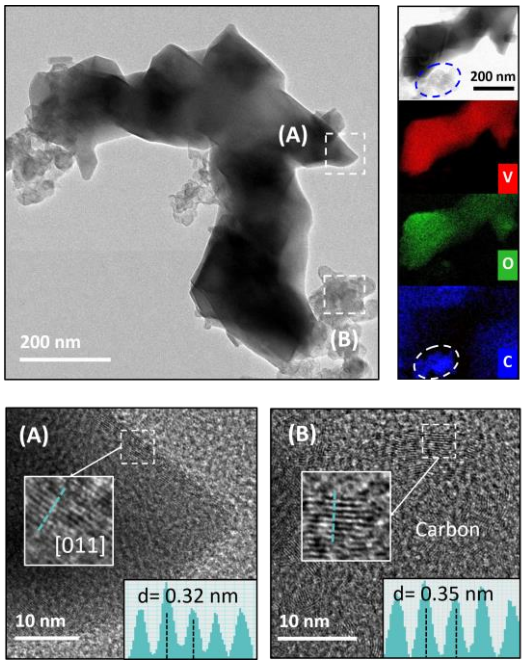

Figure. 5. Top left panel: HRTEM images of SVS-2 sample, (A) focus on one VO_2 particle and the corresponding d-spacing of 0.32 nm indexed to [011] plane, (B) focus on a soot particle showing a concentric layered architecture (onion like particle) and the corresponding spacing of 0.35 nm; Central panel: TEM images of the VO_2 and unconsumed carbon soot particles; Top right panel: TEM elemental mapping (V, O, and C elements) showing the only carbon occurrence inside the carbon soot in excess and its absence in VO_2 particles.

that excessive carbon is not used for further reduction of V (4+) to V (3+).

Moreover, these analyses show that even if 2 wt% of carbon is sufficient to transform V_2O_5 in VO_2, a slight excess of carbon needs to be introduced in order to achieve the full reduction. For avoiding too much excess of carbon, S-2 sample is chosen for further investigation.

The morphology and microstructure of SVS-2 sample after being annealed at 500°C, are shown in **Fig. 5**. Large VO_2 particles with clear boundaries, accompanied by some surrounding carbon soot nanoparticles, are observed. Specifically, in the A region, at the edge of one large crystallite, HRTEM image shows lattice fringes separated by 0.32 nm, which corresponds to [011] crystal plane of monoclinic VO_2 (M1). In the B region, the smaller particles correspond to unreacted carbon, showing the concentric network of graphene layers separated by 0.35 nm d-spacing. This analysis and so the VO_2 particles and carbon soot particle assignment are also confirmed by the elemental mapping image on the right of **Fig. 5**.

3.2. SVS and DVS processes: a comparison of the carbon-reduction mechanism

During the annealing of V_2O_5 and soot in sealed vacuum system, an interesting phenomenon was noticed that V_2O_5 can only be reduced to VO_2 at 500°C (**Fig. 3**), and V_6O_{13} impurity could not be removed totally, no matter how much carbon was added. Thus higher annealing temperatures (700°C and 1000°C) were applied to S-2 sample in both sealed vacuum and dynamic vacuum systems. The XRD pattern of the as-prepared samples are gathered in **Fig. 6**.

Using sealed vacuum system, the large decrease in VO_2 peaks intensities, such as for the main peak located at 2θ=27.95°, when the temperature increases from 500°C to 700°C, reveals that the VO_2 structure is partially destroyed, associated with an amorphisation. Indeed, the VO_2 peaks have completely disappeared at 1000°C being replaced by the ones of the V_2O_3 phase (S.G. R-3c, JCPDS No. 27-0940), suggesting the full reduction of V (4+) in V (3+) at this temperature. The obtained V_2O_3 is composed of few aggregated crystallites from a partial sintering phenomenon as shown by the electronic microscope images (**Fig. S2**).

Interestingly, annealing in dynamic vacuum system leads to a different behavior as illustrated for the DVS sample series. At 500°C, all the peaks can be indeed indexed as VO_2 (M1) phase at the exception of the occurrence of low intense peaks (located ≈ 25 °) potentially associated with some V_3O_7 impurity co-existing with the VO_2 powder. After annealing at 700°C (DVS-700) and 1000°C (DVS-1000), the XRD patterns are characteristic of a pure VO_2 (M1) phase (**Fig. 6b)**.

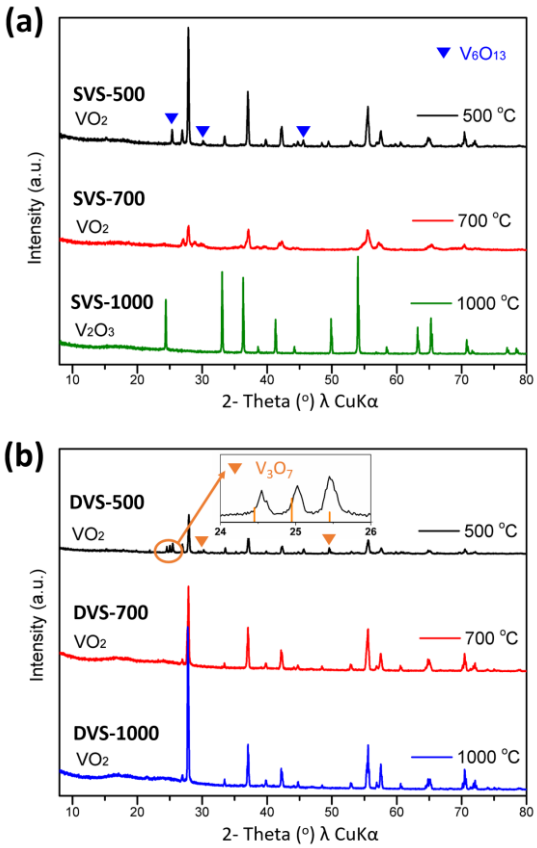

Figure. 6. (a) XRD patterns of samples obtained from annealing treatment at 500°C, 700°C and 1000°C for (a) 5 h in the sealed vacuum system; (b) 15 h in dynamic vacuum system.

Better understanding of the phase formation came from the measurements of the carbon content (**Fig. 7**) in the different samples issued from SVS and DVS annealing treatments. Before annealing, S-2 sample contains around 6.19 wt% of carbon. Surprisingly, after being annealed at 1000°C in the two vacuum systems, only little carbon content left (0.16 and 0.15 wt%), indicating that almost all the carbon took part in the reductive process. Thus the method overcomes the disadvantage of the impurity in the VO_2 product, which usually exists in redox reaction methods. [31] To explain the full mechanism in these two vacuum systems leading to different vanadium stoichiometries, two different scenarii can be proposed depending on the vacuum system (**Table 1**).

In sealed vacuum system, two mechanisms may occur either CO (**Eq. 1**) or CO_2 (**Eq. 2**) can be formed leading to different carbon percentages. Based on **Eq. 1,** at least 11.66 wt% of carbon is required with CO forming. While only 6.19 wt% of carbon is needed if the reduction goes by generating CO_2. Similarly, in dynamic vacuum system, either CO (**Eq. 3**) or CO_2 (**Eq. 4**) can be produced, corresponding to 6.19 wt% of carbon or only 3.19 wt% of carbon consumption, respectively. The loss of 6.19 wt% of carbon as determined from CHNS data (**Fig. 7**) after being annealed at 1000°C tends to favor **Eq. 2** in sealed vacuum system (*i.e.* CO_2 formation) and **Eq. 3** in dynamic vacuum system (*i.e.* CO formation).

To be consistent with our calculation, a possible formation mechanism (**Fig. 8**) is put forward. In sealed vacuum system, V_2O_5 is initially reduced to VO_2 by carbon at 500°C, generating CO gas at the same time. Since the glass tube is sealed, the CO gas cannot escape and further reacts with the new born VO_2, until all the V (4+) is fully reduced to V (3+) at 1000°C, leading to the final formation of V_2O_3 sesquioxide. The whole process is illustrated in **Fig. 8a**. On the contrary, in dynamic vacuum system, CO gas is removed out of the tube as soon as it is generated during the annealing process, preventing from any additional reduction of the new born VO_2, and corresponding to a reduction of V (5+) in V (4+) at 1000°C (**Fig. 8b**).

At 700°C in sealed vacuum system, only around 3.58 wt% of carbon is consumed. It is probably due to the fact that CO gas also takes part in the reduction of V_2O_5 to VO_2 and VO_2 to V_2O_3, explaining the poor crystallinity of VO_2 (SVS-700 in **Fig. 6a**). As a comparison, almost all the carbon is consumed in dynamic vacuum system. In that case, CO gas is removed quickly preventing from any additional reduction, the carbon act as the only reducing agent, leading to the desired formation of a pure VO_2 dioxide.

To obtain pure VO_2 powder with high crystallinity, it is imperative to avoid the second reductive step of vanadium oxides linked to the oxidation of CO in CO_2 during the annealing treatment at high temperatures. Pure VO_2 (M1) particles can be synthesized in dynamic

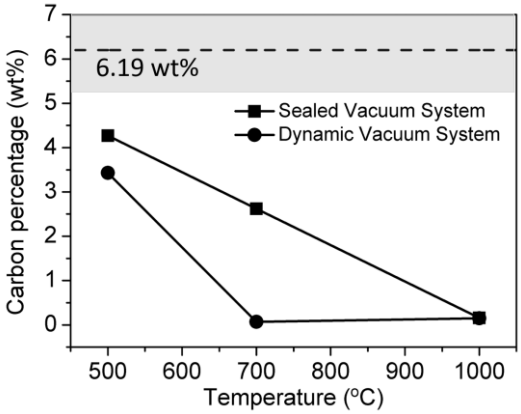

Figure. 7. Carbon wt. content of samples after annealing using two types of vacuum systems, namely sealed vacuum system (SVS) and dynamic vacuum system (DVS). (The dash line is the guideline standing for 6.19 wt% carbon in the mixed powder before annealing).

	Equations	$\frac{m(C)}{m(V_2O_5)+m(C)}$
SVS	$V_2O_5 + 2C \rightarrow V_2O_3 + 2CO$ ….. $Eq.\ 1$	*11.66%*
	$V_2O_5 + C \rightarrow V_2O_3 + CO_2$ ….. $Eq.\ 2$	*6.19%*
DVS	$V_2O_5 + C \rightarrow 2VO_2 + CO$ …… $Eq.\ 3$	*6.19%*
	$2V_2O_5 + C \rightarrow 4VO_2 + CO_2$. …. $Eq.4$	*3.19%*

Table. 1. Possible equations taking place in sealed or dynamic vacuum systems, and the associated calculated carbon weight percentage needed considering stoichiometric proportion.

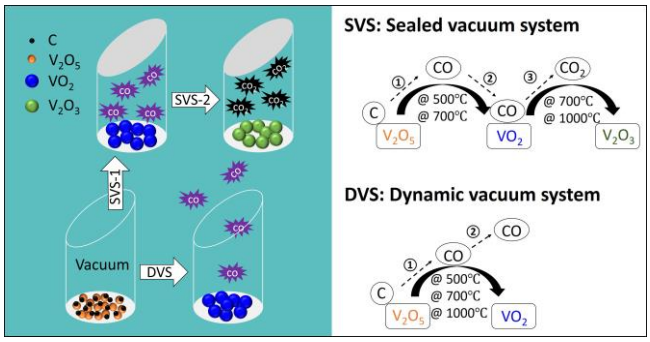

Figure. 8. Schematic illustration of possible reactions occurring in the SVS: sealed vacuum system and in the DVS: dynamic vacuum system.

vacuum system at 700°C and 1000°C successfully, thanks to the extraction of the CO from the synthesis chamber.

3.3. Physical-chemical properties of the as-prepared VO_2 (M1) compounds

XRD patterns of the VO_2 compounds obtained using DVS treatments were refined using the Fullprof software program, to determine the structural parameters of the as-obtained oxides: unit-cell parameters, atomic positioning, *etc*. The results are presented in **Fig. S4**. The crystal structure corresponding to the diffraction patterns well correspond to the monoclinic phase of VO_2 (M1 phase) (S.G. $P2_1/C$, JCPDS No. 44-0252), with standard lattice parameters and atomic positions (**Table. S1** and **Table. S2**).

The morphologies and microstructures of DVS-700 and DVS-1000 samples are firstly investigated by SEM (**Fig. 9**), the corresponding

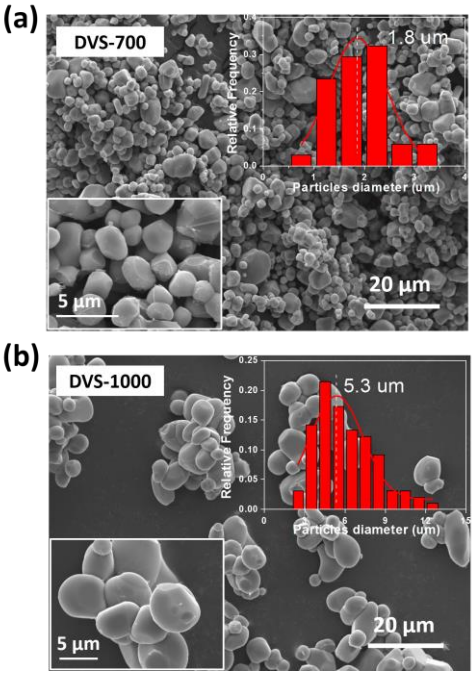

Figure. 9. SEM images of the as-synthesized VO_2 (M1) particles: (a) DVS-700 and (b) DVS-1000 samples. In inset is reported the corresponding particle size distribution.

size distributions are added in the inset of **Fig. 9**. Both powders show an isotropic shape. For the DVS-700, the size distribution, which is clearly a single-mode Gaussian distribution, is centered on 1.8 µm **(Fig. 9a)**. The distribution width enlarges and the average size increases to 5.3 µm when the annealing treatment is 1000°C, as shown in **Fig. 9b**.

High temperature will lead to a highly crystallized VO_2 (M1), which is more favorable because of its stability, while the particle size will also increase. To overcome such disadvantage, the time of the annealing treatment can be decreased allowing a good control of the average grain size. Indeed, the average size of the synthesized VO_2 particles is greatly decreased to 935 nm and 415 nm for an annealing temperature of 700°C when the annealing time is shortened to 2 h and 1 h, respectively (**Fig. S4**). Xiao et al reported that it is known that the VO_2 particles are relatively uniform (in terms of shape and size distribution width) when an annealing temperature higher than 500°C is used. [32] For samples annealed at 700°C, the size of single particle is larger than 500 nm. This past research is in good agreement with our own experiments. Unlike the belt-like or rod-like VO_2 morphologies synthesized from intermediated phase transformation, [31] which are unfavorable for the dispersion in aqueous solvent, the obtaining of isotropic VO_2 particles with a narrow distribution width, is well adapted to their dispersion into suspension which could be used to elaborate homogeneous films from dip coating process.

More detailed structural information on the synthesized VO_2 powder is obtained from high resolution TEM. A focus was made especially for the DVS-700 sample as shown in **Fig. 10a**. The vanadium atomic columns are clearly visible and the V-V distance is extracted around 0.35 nm (**Fig. 10b-c**), which is fully consistent with

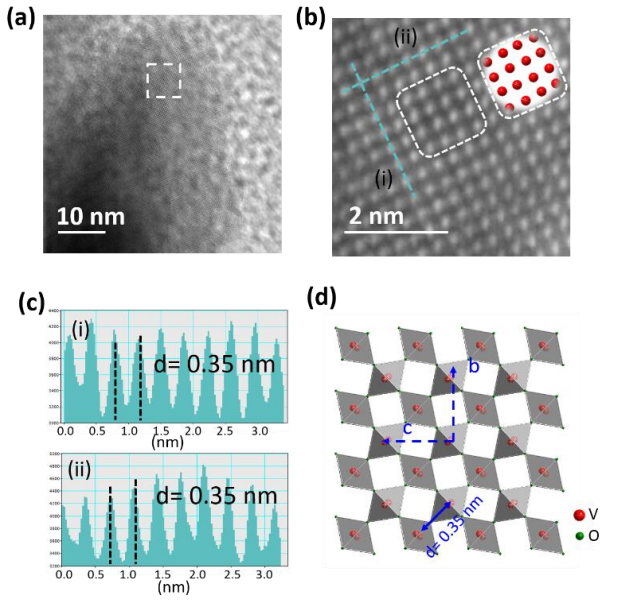

Figure. 10. (a) HRTEM image of VO_2 (M1) powder (DVS-700); (b) Enlargement of the HRTEM image showing V-V atomic distances and illustration of the perfect matching with the VO_2 crystal structure along [100] zone axis. (c) The crystal structure of monoclinic VO_2 (M1) from Diamond with same projection axis.

the shortest V-V atomic distance in the VO_2 (M1) crystal structure (**Fig. 10d**).

The awaited phase transition between monoclinic phase (low temperature form) and rutile phase (high temperature form) for the

as-prepared VO_2 compounds is investigated through its latent heat (thanks to DSC measurements) and the drastic change of electronic conductivity associated with this MIT phase transition (four probes measurements *versus* temperature on VO_2 pellets).

The DSC analysis is shown in **Fig. 11a**. The endothermic and exothermic peaks during heating and cooling cycles are clearly visible, which shows a transition temperature of about 61°C in cooling mode and 70°C in heating mode, whatever the samples: DVS-700 or DV-S1000, *i.e.* with a hysteresis loop width of about 10°C. The phase change enthalpy (ΔH) during the heating cycle and cooling exhibited a considerably high value nearly 55 J/g, a bit larger than the value of 51 J/g for bulk VO_2 previously reported in literature. [33] The high enthalpy could be attributed to the well crystallized VO_2 (M1) obtained from the high annealing temperature. The ratio of ΔH_H and ΔH_C is 1.012 (54.259/53.612) for DSV-700 sample, and 1.016 (55.254/54.362) for DSV-1000 sample. The ratios are quite close to 1, which implies the excellent reversibility of the phase transition for these samples thanks to their good crystallinity.

Resistivity measurements on DVS-700 and DVS-1000 samples, reported in **Fig. 11b,** show that the DVS-700 gets a change of resistivity of about 3 orders of magnitude between the insulating

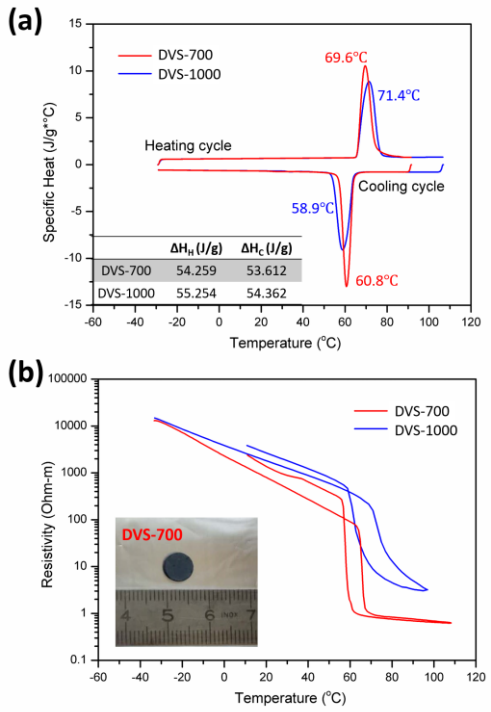

Figure. 11. Phase transition behavior of synthesized VO_2 (M1) (DVS-700 and DVS-1000): (a) Their corresponding DSC curve; (b) Electrical resistance of the VO_2 (M1) pellets; the heating and cooling rate for all measurements is set as 5 °C/min.

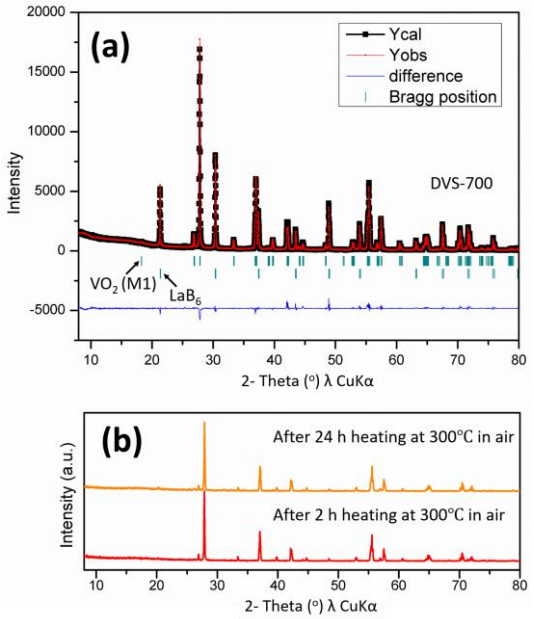

Figure. 12. (a) Typical Rietveld refinements of XRD data from DVS-700 sample mixed with LaB_6; (b) XRD pattern of DVS-700 after annealing at 300°C in air for 2 h and 24 h.

and the metallic forms whereas the DVS-1000 only show a jump of 2 orders of magnitude when the sample is cooled down. In agreement with DSC result, a 10°C hysteresis width is measured for both samples between cooling and heating modes. The M1-R transition is usually accompanied by a 3-6 orders of magnitude jump in conductivity. The typical curves for our samples are in substantial agreement with published results. [25, 34] The DVS-1000 sample shows a poor transition behavior, probably because of the larger particle size (~5.3 µm) that makes difficult to prepare a quite dense pellet and can be at the origin of new cracks formation during the measurements; the observation of a higher resistivity of the DVS-1000 pellet whatever the temperature is and so the allotropic form in comparison with the DVS-700 pellet, tends to validate this interpretation.

As shown from Rietveld analysis of the XRD pattern of a mixture of 90 % VO_2 (DVS-700) and 10 % lanthanum hexaboride, the DVS-700 VO_2 (M) powder is of high purity (100 % monoclinic phase) and of high crystallinity **(Fig. 12a)**. Such characteristics are essential for ensuring good stability as confirmed by the XRD pattern after 24 hrs annealing at 300 °C in air **(Fig. 12b).** It is worth mentioning that after similar annealing process, Fu *et al* observed a transformation into V_2O_5 after only two hours for poorly crystallized VO_2 films. [35]

3.4. M-doped VO_2 with M = Ti or Al.

10 mol% Al-doped VO_2 and Ti-doped VO_2 powders were prepared at 700°C for 5 h using the DVS system in order to be compared with the undoped DVS-700 sample. With the designed target composition of 10 at% doping, ICP-OES measurement shows the real doping content are 1.18 wt% and 4.37 wt% for Ti-VO_2 and Al-VO_2 sample.

X-ray diffraction pattern of the obtained powders are reported in **Fig. 13a**. The Ti-doped VO_2 phase exhibits only peaks associated with the M1 monoclinic phase whereas M2 phase can be detected when the vanadium is substituted with Al^{3+} dopant. Intriguing, M2 phase is a Mott insulator, which can transform to metallic M2 upon carrier

injection, showing potential applications in Mott field-effect transistor. It has already been reported in literature, [36] that the introduction of aluminum inside the VO_2 crystal framework allows the stabilization of the M2 allotropic form. Thus, the synthesis process herein used is able to provide a controllable and reliable method for producing M2 phase.

Fig. 13b shows DSC curves of the two doped samples, which corresponding to the M1-R for transition for Ti-VO_2 and M1-M2-R multiple transition for Al-VO_2.

The Ti-VO_2 shows unclear (non-significant) changes comparing with the pure VO_2 (DSV-700), in good correlation with literature reporting either a very slight decrease of the transition temperature versus Ti-doping, [37, 38] or a very slight increase of this temperature. [39, 40] Moreover, a careful comparison of the DSC curves of the undoped and Ti-doped samples indicates that (i) the enthalpies are non-significantly impacted, (ii) the hysteresis loop tends to slightly enlarge and especially, (iii) the temperature range on which occurs the transition for both cooling and heating modes becomes wider (the DSC peaks are larger, the transition becomes smoother) while Ti^{4+} ions are introduced in the VO_2 crystal network.

For Al-doping, the most interesting aspect is that the occurrence of a M1-M2-R multiple transition while Al^{3+} ions are introduced in VO_2 modifies the DSC peak from a single peak to a quite convoluted but clearly observable doublet, well illustrating the pathway through an intermediate phase, namely the M2 phase. Also, the phase change enthalpy (ΔH) decreases clearly after doping, which can be ascribed to the large local distortions inside the host monoclinic VO_2 matrix resulting from the aliovalent substitution of V^{4+} with Al^{3+} and/or by an "accommodation" of the phase transition from the occurrence of the intermediate allotropic form (M2 phase).

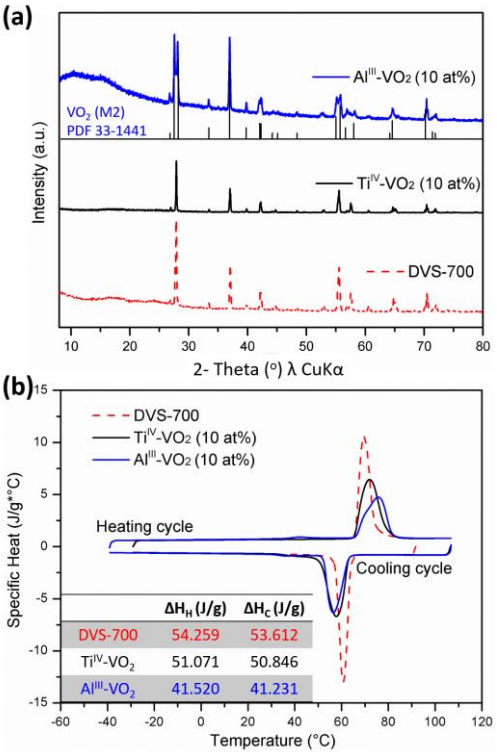

Figure 13. (a) XRD patterns of the Ti-VO_2 and Al-VO_2, in comparison with DVS-700. (b) DSC curves of the corresponding doped VO_2 samples. For simplification, the target composition of 10 % is indicated.

Conclusions

A method of synthesis of VO_2 (M1) powder is developed and investigated by using soot to reduce V_2O_5. Two types of vacuum systems are designed and applied to study the mechanism of the reductive process. In the sealed glass system, two reducing steps are involved: carbon reduces V_2O_5 with CO gas generating simultaneously, the CO gas continues in a second step to reduce the new born VO_2, leading to the formation of V_2O_3 at 1000°C. As a comparison, the use of the dynamic vacuum system, while CO gas is removed directly in order to avoid the second step of the reductive process, guarantees the single formation of VO_2 at high annealing temperatures (700°C and 1000°C). The mechanism is confirmed by the carbon content measured before and after annealing. Hence, with the help of carbon, VO_2 (M1) powders with high crystallinity are synthesized successfully at 700°C (DVS-700) and 1000°C (DVS-1000). Their morphologies are compared through SEM, displaying the occurrence of particle sets with isotropic and narrow size distribution and with an average particle size which can be easily controlled in a large range via the synthesis parameters: time and temperature of annealing, between 400 nm and more than 5 µm. Both DSC and conductivity show the phase transition behavior and let open thermochromic applications. Finally, an important finding is that this method also provides the possibility for Ti and Al doping allowing the control of the phase transition parameters. Further doping including W^{6+} and Nb^{5+} ions, which are known to drastically decrease the phase transition temperature and so increase the potentialities for the use of such thermochromic compounds for thermal insulation improvement of smart windows, is currently under investigation and will be the content of a forthcoming paper.

Conflicts of interest

There are no conflicts to declare.

Acknowledgements

The authors would like to thank Eric Lebraud, Sonia Buffière, Giljoo Song, Laetitia Etienne, Dominique Denux for their assistance during XRD, SEM & TEM, CHNS and DSC measurements. All authors contributed to the discussions and revisions of the manuscript.

Notes and references

1 F. J. Morin, *Phys. Rev. Lett*., 1959, **3**, 34.
2 Y. Choi, D. Sim, Y. H. Hur, H. J. Han and Y. S. Jung, *Sol. Energy Mater. Sol. Cells.,* 2018, **176**, 266.
3 S. M. Babulanam, T. S. Eriksson, G. A. Niklasson and C. G. Granqvist, *Sol. Energy Mater.*, 1987, **16**, 347.
4 F. Xu, X. Cao, H. Luo and P. Jin, *J. Mater. Chem. C.*, 2018, **6**, 1903.

5 K. Liu, S. Lee, S. Yang, O. Delaire and J. Wu, *Mater. Today*., 2018, DOI: 10.1016/j.mattod.2018.03.029.dioxide.
6 J. H. Son, J. Wei, D. Cobden, G. Cao, and Y. Xia. *Chem. Mater*., 2010, **22**, 3043.
7 A. Gonçalves, J. Resende, A. C. Marques, J. V. Pinto, D. Nunes, A. Marie, R. Goncalves, L. Pereira, R. Martins and E. Fortunato, *Sol. Energy Mater. Sol. Cells*., 2016, **150**, 1.
8 G. R. Mutta, S. R. Popuri, M. Vasundhara, M. Maciejczyk, A. V. Racu, R. Banica, N. Robertson, J.B. Wilson and N. S. Bennett, *Mater. Res. Bull.,* 2016, **83**, 135.
9 J. Hou, Z. Wang, Z. Ding, Z. Zhang and J. Zhang, *Sol. Energy Mater. Sol. Cells.,* 2018, **176**, 142.
10 [T. Suetsugu, Y. Shimazu, T. Tsuchiya, M. Kobayashi, M. Minohara, E. Sakai, K. Horiba, H. Kumigashira, and T. Higuchi, *Jpn. J. of Appl. Phys.,* 2016, **55**, 06GJ11.
11 N. H. Azhan, K. Su, K. Okimura, M. Zaghrioui, and J. Sakai. *Jpn. J. of Appl. Phys.,* 2015, **117**, 245314.
12 C. Batista, R. M Ribeiro and V. Teixeira, *Nanoscale. Res. Lett.,* 2011, **6**, 301.
13 C. Drosos and D. Vernardou, *Mater.,* 2018, **11**, 384.
14 D. Graf, J. Schlafer, S. Garbe, A. Klein, and S. Mathur. *Chem. Mater.,* 2017, **29**, 5877.
15 M. Wan, B. Liu, S. Wang, L. Hu, Y. He, H. Tao and X. Zhao, *J. Alloy. and Compd.,* 2017, **706**, 5, 289.
16 S. Dou, Y. Wang, X. Zhang, Y. Tian, X. Hou, J. Wang, X. Li, J. Zhao and Y. Li. *Sol. Energy Mater. Sol. Cells*., 2017, **160**, 164.
17 I. G. Madida, A. Simo, B. Sone, A. Maity, J.B. Kana Kana, A. Gibaud, G. Merad, F.T. Thema and M. Maaza, *Sol. Energy*., *2014,* **107**, 758.
18 Y. Gao, S. Wang, H. Luo, L. Dai, C. Cao, Y. Liu, Z. Chen and M. Kanehir, *Energy Environ. Sci*., 2012, **5**, 6104.
19 Qinghong Wang, Jiantie Xu, Wenchao Zhang, Minglei Mao, Zengxi Wei, Lei Wang, Chunyu Cui, Yuxuan Zhu and Jiamin Ma, J. Mater. Chem. A, 2018, **6**, 8815-8838;
20 B. Belbeoch, R. Kleinberger and M. Roulliay, *J. Phys. Chem. Solids*., 1978, **39**, 1007.
21 P. L. Gai, *Philos. Maga. A* ., 1983, 48. 3.
22 N. Kimizuka, M. Ishii. Isao Kawada, M. Saeki and Mitsuoki Nakahira, *J. Solid. State Chem*., 1974, **9**, 69.
23 C. Tsang and A. Manthiram, *J. Electrochem. Soc*., 1997, **144**, 520.
24 H. Zhang, X. Xiao, X. Lu, G. Chai, Y. Sun, Y. Zhan and G. Xu, *J. Alloy. and Compd.,* 2015, **636**, 106.
25 I. Mjejri, A. Rougier, and M. Gaudon, *Inorg. Chem.,* 2017, **56**, 1734.
26 S. Guan, A. Rougier, O. Viraphong, D. Denux, N. Penin, and M. Gaudon, *Inorg. Chem.*, 2018, ***57***, 8857.
27 E. Strelcov, A. Tselev, I. Ivanov, J.D. Budai, J. Zhang, J. Z. Tischler, I. Kravchenko, S. V. Kalinin, and A. Kolmakov. *Nano Lett.,* 2012, **12**, 6198.
28 N. F. Quackenbush, H. Paik, M. J. Wahila, S. Sallis, M. E. Holtz, X. Huang, A. Ganose, B. J. Morgan, D. O. Scanlon, Y. Gu, F. Xue, L. Q. Chen, G. E. Sterbinsky, C. Schlueter, T. L. Lee, J. C. Woicik, J. H. Guo, J. D. Brock, D. A. Muller, D. A. Arena, D. G. Schlom, and L. F. J. Piper, *Phys. Rev. B.,* 2016, **94**, 085105.
29 M. Pawlyta and H. Hercman, *Ann. Soc. Geol. Pol.,* 2016, **86**, 00.
30 Y. J. Ko, K. Choi, J. Y. Kim, I. Kim, D. S. Jeong, H. J. Choi, H. Mizuseki and W. S. Lee, *Carbon*., 2018, **127**, 31e40.
31 Y. Cui, Y. Ke, C.Liu, Z. Chen, N. Wang, L. Zhang, Y. Zhou, S. Wang, Y. Gao and Y. Long. *Joule*., 2018, DOI: 10.1016/j.joule.2018.06.018.
32 X. Xiao, H. Zhang, G. Chai, Y. Sun, T. Yang, H. Cheng, L. Chen, L. Miao and G. Xu. *Mater. Res. Bull.,* 2014, **51**, 6.
33 Z. Chen, Y. Gao, L. Kang, C. Cao, S. Chen and H. J. Luo, *J. Mater. Chem. A*., 2014, **2**, 2718.
34 C. J. Dahlman, G. LeBlanc, A. Bergerud, C. Staller, J. Adair, and D. J. Milliron, *Nano Lett*., 2016, **16**, 6021.
35 G. H. Fu, A. Polity, N. Volbers and B. K. Meyer, *Thin Solid Films*., 2006, **515**, 2519.
36 Y. Wu, L. Fan, S. Chen, S. Chen, F. Chen, C. Zou and Z. Wu. *Mater. Lett.,* 2014, **127**, 44.
37 C. N. R. Rao, M. Natarajan, G. V. S. Rao and R. E. Loehman, *J. Phys. Chem. Solids*., 1971, **32**, 1147.
38 M. Nishikawa, T. Nakajima, T. Kumagai, T. Okutani and T. Tsuchiya, *J. Ceram. Soc. jpn.,* 2011, **119**, 577.
39 Y. Hu, Q. Shi, W. Huang, H. Zhu, F. Yue, Y. Xiao, S. Liang and T. Lu, *J. Sol-Gel Sci Technol.,* 2016, **78**, 19.
40 S. C. Barron, J. M. Gorham, M. P. Patel and M. L. Green, *ACS Comb. Sci.,* 2014, **16**, 526.